

Soft, Thiol-ene/Acrylate-Based Electrode Array for Long-Term Recording of Intracranial EEG Signals with Improved Biocompatibility in Mice

Flóra Zsófia Fedor, Miklós Madarász, Anita Zátanyi, Ágnes Szabó, Tibor Lőrincz, Vindhya Danda, Lisa Spurgin, Connie Manz, Balázs Rózsa, and Zoltán Fekete*

Thiol-ene/acrylate, a softening polymer material, rapidly gained attention during the past few years as a substrate of intracortical probes, as soft polymers can mitigate foreign body response by reducing mechanical mismatch between the neural implant and the surrounding brain tissue. This paper presents a comprehensive analysis of a thiol-ene/acrylate based microECoG (micro – electrocorticography, μ ECoG) device with 31 sputtered iridium oxide electrodes. Long-term electrochemical measurements provide firm evidence on the reliability of the novel layer structure and the related packaging method. In vivo impedance measurements indicated stable electrode yield (over 75%), without apparent signs of delamination or material degradation over 75 days. Awake recordings of theta oscillations with signal-to-noise ratio between 1.04 and 5.74 over this extended period also confirmed the applicability of the device. Chronic immune response characterized by Glial Fibrillary Acidic Protein staining of astrocytes and fluorescent Nissl (NeuroTrace) staining of neurons revealed only modest foreign body reaction after 80 days of implantation. The study presents novel data that confirms the feasibility of softening polymer-based μ ECoG devices as chronically implantable neural interfaces.

surgical resection to avoid healthy brain tissue. ECoG devices record neural activity directly on the cortical surface, featuring invasiveness between electroencephalographic (EEG) recording devices and penetrating intracortical probes. ECoG signals are rich in frequency components that are difficult to record in a reliable manner with EEG due to the filtering properties of the skull, the subcutaneous tissue and the scalp.^[1] These frequency components cover the gamma bandwidth, which correlates with large scale brain networks, for example sensory—motor activity and cognitive functions such as memory.^[2–5] Microfabrication processes allow the fabrication of structurally diverse interfaces with densely packed recording sites,^[6–9] enabling ECoG to surpass EEG with its higher spatial resolution and better signal-to-noise ratio (SNR). ECoGs designed for experimental and clinical studies may help to understand how the brain processes

1. Introduction


Advances in electrophysiology enabled electrocorticography (ECoG) to become a standard tool for clinical presurgical localization of epileptogenic brain tissue and for guidance during

information through revealing functional connectivity patterns, therefore they are promising candidates for brain–computer interfacing (BCI) technology.^[10]

Stress from micromotions (induced by breathing, heartbeat, brain pulsation, circulation, etc.) has been implicated as the

F. Z. Fedor, A. Zátanyi, Á. Szabó, Z. Fekete
Research Group for Implantable Microsystems
Faculty of Information Technology & Bionics
Pázmány Péter Catholic University
Budapest H-1088, Hungary
E-mail: feketezoltan@itk.ppke.hu

F. Z. Fedor
Microsystems Laboratory
Centre for Energy Research
Budapest H-1121, Hungary

 The ORCID identification number(s) for the author(s) of this article can be found under <https://doi.org/10.1002/admt.202100942>.

© 2021 The Authors. Advanced Materials Technologies published by Wiley-VCH GmbH. This is an open access article under the terms of the Creative Commons Attribution License, which permits use, distribution and reproduction in any medium, provided the original work is properly cited.

DOI: 10.1002/admt.202100942

F. Z. Fedor
Doctoral School of Chemical Engineering and Material Sciences
University of Pannonia
Veszprém H-8200, Hungary

M. Madarász
János Szentágothai PhD Program of Semmelweis University
Budapest H-1085, Hungary

M. Madarász, T. Lőrincz, B. Rózsa
Laboratory of 3D functional network and dendritic imaging
Institute of Experimental Medicine
Budapest H-1083, Hungary

Á. Szabó
Roska Tamás Doctoral School of Sciences and Technology
Pázmány Péter Catholic University
Budapest H-1088, Hungary

V. Danda, L. Spurgin, C. Manz
Qualia Labs, Inc.
Dallas, TX 75252, USA

main reason for neuroinflammatory response during prolonged presence of μ ECoGs, which may result in glial scar formation and finally the encapsulation of the artificial system.^[11–13] In chronic experiments, encapsulation of neuroprostheses will lead to unreliable electrical recordings, unstable signal quality over the extended period, and eventually resulting in impedance increase or even loss of functionality due to the spatial and electrical insulation from active neuronal ensembles.^[14,15] Previous research suggests that mechanically compliant neural interfaces that conform better to the curvilinear surface of the brain would be more likely to reduce stress at the biotic–abiotic interface.^[13,16,17] Diverse strategies have been discovered and exploited to soothe foreign body reaction by replacing rigid materials with more compliant alternatives or by temporarily covering rigid silicon backbones with soft bioresorbable polymer materials.^[18,19] Recent studies have employed various flexible polymer materials^[20] as substrates for the fabrication of μ ECoG devices, for example polyimide,^[21–24] poly(p-xylylene) with different functional groups, such as Parylene C^[7,25–27] and Parylene HT,^[9] SU-8,^[24,28] and silicone rubber,^[29] especially Silastic,^[30] a material approved by the United States Food and Drug Administration for human research. Baek et al.^[31] and Rubehn et al.^[32] fabricated a multichannel, flexible μ ECoG electrode array with a mesh-form structure of open interelectrode spaces, or fenestrae to enhance the contactability with the curvilinear surface of the brain. Unfortunately, elastic properties of the mentioned thin polymer interfaces are still significantly different from the neural tissue.^[16] The reduction of mechanical mismatch can be attained via a variety of routes, including bioresorbable polymer materials (e.g., silk,^[33,34] poly(lactic-co-glycolic acid) (PLGA)^[19]), mechanically adaptive substrates (e.g., hydrogel^[35]), and with the application of fenestrae or aperture that disrupt the consistency of the device structure.^[36] These attempts are either trying to approximate the Young's modulus of the device to the surrounding tissue or increase the compliance by forming mesh-like structures. For instance, Wu et al.^[22] facilitated the implantation with a bioresorbable substrate of silk fibroin. After the μ ECoG device is implanted, the silk starts to dissolve in the physiological environment, and eventually only the thin and conformal polyimide base structure will remain at the biotic–abiotic interface. Watanabe et al.^[34] also applied bioresorbable PLGA in 30 μ m thickness, which formed the substrate of an actively multiplexed neural electrode array. Although the hydrolytic degradation of bioresorbable polymers from natural materials result in the formation of nontoxic species only,^[37] their neural applications are still questionable due to the small time window of operation. The group of mechanically adaptive materials constitutes of softening polymers (or shape memory polymers, SMP), e.g., thiol-ene/acrylate thermoset polymers^[38–41] and hydrogels^[19,42,43] (from natural materials e.g. collagen I, collagen I—fibronectin, alginate, chitosan or from synthetic materials, e.g., polyglycolic acid (PGA), polyethylene glycol (PEG), polyvinyl alcohol (PVA). Newly engineered softening polymer materials transition in response to stimuli (e.g. temperature, ion concentration, pH, aqueous environment) when they are exposed to the extracellular space. Like hydrogels, softening polymer materials maintain their mechanical robustness (Young's modulus in the GPa range) during implantation, thus providing easy handling before and after neurosurgeries.

Thiol-ene/acrylate compositions have been shown to undergo remarkable changes in their elastic properties, softening from over 1 GPa to 300 MPa with less than 3% fluid uptake upon exposure to 37 °C in phosphate buffered saline (PBS).

While currently available electrophysiological (e.g., ECoG) and neuroimaging methods might approach their spatiotemporal resolution due to biological and technical considerations, integration of multiple and complementary techniques in an attempt to leverage the temporal resolution of electrophysiology and the spatial resolution of neuroimaging is expected to receive great interest in the near future. Understanding the relationship between anatomical and functional neural connectivity is essential for both diagnostic and therapeutic applications, such as a neuroprosthetic interface to restore lost motor functions in paralyzed patients. Although the implantation of μ ECoGs is less invasive to the brain tissue, it has been reported that μ ECoG devices do induce foreign body reaction—the specific immune response of the nervous system to implanted neuroprostheses.^[44,45]

Based on the above mentioned reasons, we designed a thiol-ene/acrylate based μ ECoG device. We hypothesized that by using a softening polymer as a substrate, the device will better fit to the curvilinear surface of the brain, which would reduce the foreign body related immune response. In the present article, we demonstrate the in vivo functionality of our μ ECoG device by recording extracellular activity from cortical regions in awake mice. To assess whether the subdurally implanted μ ECoG array is viable with respect to the chronic foreign body reaction, immunohistochemical analysis of the stained cortical tissue was carried out focusing on astrocytes and the physiological state of neurons after 80 days of implantation.

2. Experimental Section

2.1. Design, Fabrication, and Packaging

Composition and synthesis of the thiol-ene/acrylate polymer substrate is described in the prior work.^[39] The μ ECoG device is designed to be used with ease in chronic mouse experiments, where challenges of limited space and weight need to be addressed. Since the future aim is to make this device compatible with neuroimaging techniques through a cranial window, a symmetric layout including 31 recording sites was defined. The final device is shown on **Figure 1A**. First and last rows of the array are composed of three channels, while five rows in between consist of five channels, all equally distant from neighboring electrodes. The electrode diameter and the electrode-to-electrode distance are 115 and 400 μ m, respectively. The overall thickness of the device is \approx 14 μ m in the SMP only regions and \approx 18 μ m over the traces (see **Figure 1C**). The microfabrication process, which was carried out at Qualia Labs, Inc., relies on the micromachining scheme of the intracortical probe published earlier.^[39] Briefly, a thiol-ene/acrylate based SMP substrate with 2 μ m Parylene C encapsulation around the traces was used. Devices were photolithographically patterned with 400 nm thick gold and 300 nm thick sputtered iridium oxide (SIROF). The scheme of the layer composition of the device including dimensions is shown in **Figure 1C**. When microfabrication steps were

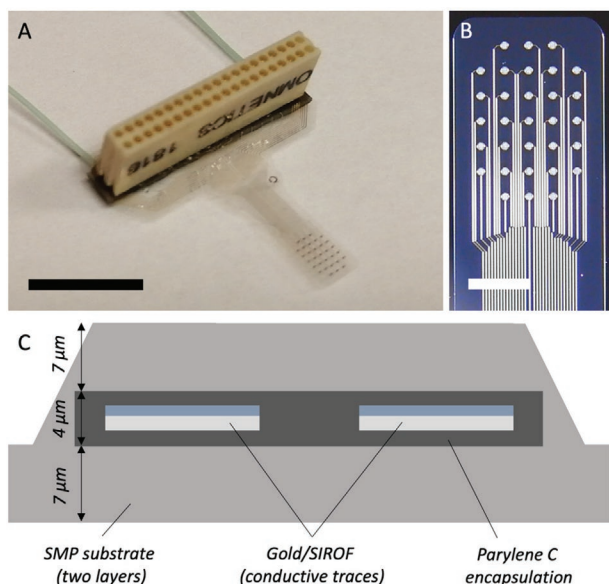


Figure 1. A) Photo on the ready-to-use thiol-ene/acrylate based μ ECoG device and B) top microscope view on the recording array. Scale bars show 5 and 1 mm, respectively. C) A schematic (not to scale) presenting a cross-sectional view of the layer composition of the device.

finished, devices were mounted on a through-hole Omnetics connector (A79022-001, Omnetics Connector Corp., USA). Interconnection between the integrated conductive traces and the connector pins were made through two-component conductive epoxy (CW2400, Chemtronics, USA), which was dried at room temperature for 24 h. To encapsulate the through-hole joints, they were fully coated with Araldite 1401 adhesive (Huntsman Advanced Materials, TX), which was also cross-linked without using any thermal annealing process.

2.2. Evaluation of Electrochemical Properties

In order to test the long term encapsulation stability of thiol-ene/acrylate based μ ECoG devices before in vivo experiments, Bode plots of each SIROF recording site were recorded using electrochemical impedance spectroscopy (EIS). The main components of the three-electrode electrochemical cell include 0.01 M PBS solution (P4417, tablet diluted in 200 mL distilled water, pH 7.4, Merck KGaA, Germany), platinum wire as counter, Ag/AgCl as reference electrode (ET072-1, eDAQ Pty Ltd., Australia), and electrode sites of each μ ECoG device. EIS measurements were performed using a Gamry Reference 600+ Potentiostat (Gamry Instruments, Warminster, PA) at 25 mV rms across a frequency range from 1 Hz to 10 kHz during 16 days of soaking experiment on two different but functionally equal μ ECoG arrays. Bode plots were recorded immediately after arrays were submerged in PBS solution and thereafter on a daily basis. Data were analyzed and the equivalent circuit parameters were fitted with Gamry Echem Analyst software (Gamry Instruments, Warminster, PA). To obtain better curve fitting, the common Randles circuit was extended with a capacitive parameter (Figure S1, Supporting Information), which represented the porous surface of SIROF electrodes. EIS measurements

were conducted in a Faraday-cage. μ ECoGs, evaluated with EIS, were exclusively used in in vitro experiments.

2.3. In Vivo Experiments and Surgery

All mice used in this study were in-house bred from C57BL6/J strain. All experiments were conducted in compliance with the EU directive in force (2010/63/EU) in accordance with the applicable national government decree (40/2013.(II. 14.)), and were approved by the National Food Chain and Safety Office (PE/EA/776-5/2021).

2.3.1. Surgery

Three adult male C57BL6/J mice were used in total. ECoG device, reference electrode and headbar implantation were carried out in a single surgery. Mice were anesthetized with fentanyl (0.05 mg kg^{-1}), medetomidine (0.5 mg kg^{-1}), midazolam (5 mg kg^{-1} , i.p. and ropivacaine (5 mg kg^{-1} , subcutaneously) was used for local analgesia. Eye ointment (Opticorn A) was applied, and the surgical area was disinfected with Betadine. Skin on the top of the skull was removed and the underlying bone was cleaned with 3% H_2O_2 . The boundary of a rectangular craniotomy 2.5 by 3.8 mm in size was marked on the bone, with the sagittal suture and one of the short edges enclosing an angle of $\approx 27^\circ$ and the two vertices of this short edge positioned against the sagittal and lambdoid sutures. The craniotomy was performed with a 0.3 mm burr bit (1AU, Busch & CO). On the edge where the device would exit the craniotomy, a bone ramp was formed for smoother placement. Sterile tampons (Gelita, BBraun) soaked in Ringer's solution were used for constant hydration. After the dura was removed, the device was placed on the brain surface and covered with two custom-cut glass coverslips (inner: 2.5 by 3.8 mm, outer: 3.2 by 4.2 mm, 0.15 mm thick), joined by optical adhesive (NOA71, Norland). The covering glass was glued to the bone, sealing the craniotomy. After curing, the connector was fixed to the skull in a separate step, and exposed parts of the substrate were also covered with glue. An epidural reference electrode was implanted over the left side of the cerebellum (see Figure 2). A mixture of dental cement (Relyx Luting cement, 3M) and quick curing glue (Super Bond Gel, Loctite) was used in these steps. A steel headbar was fixed to the skull anterior to the craniotomy with dental adhesive (Super-Bond C&B). Surgery involved the implantation of glass coverslip and the steel headbar in order to perform measurements combined with two-photon microscopy, which will be presented in a following article. Revertor (2.5 mg kg^{-1}), flumazenil (2.5 mg kg^{-1}), and nexodal (1.2 mg kg^{-1}) were administered i.p. to wake the mice, as well as melosolute (0.2 mg kg^{-1}) for analgesia and Ringer's solution for hydration. Mice were allowed to rest for at least 3 days before starting the measurements.

2.3.2. Electrophysiological Measurements

1 week after surgery, mice were head-fixed on a rotary treadmill recording their movement speed. The implanted device

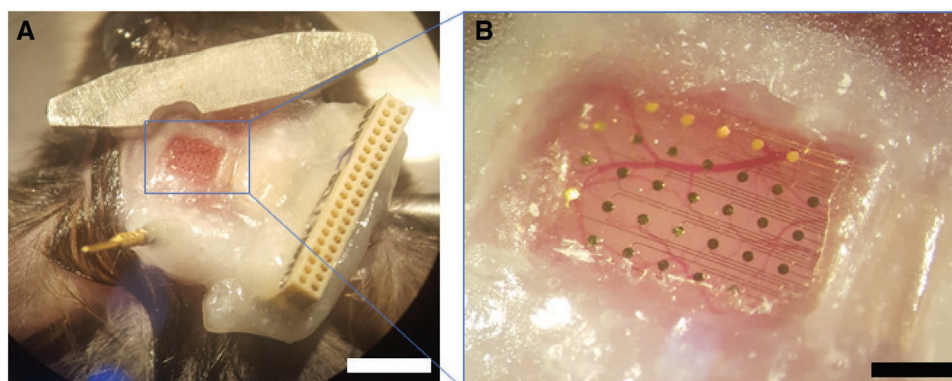


Figure 2. A) Surgical arrangement of the device on the top of the cortical surface. B) Position of SIROF recording sites compared to cortical vascularization. Scale bars show 5 and 1 mm, respectively.

was connected to a 32-channel RHD recording headstage and RHD2000 Evaluation system (INTAN Technologies). Electrode impedance was measured between 1 and 5000 Hz weekly. Sample brain activity was also measured from all 31 recording sites at 2 kHz sampling rate. After data from 10 measurements were collected, mice were sacrificed and processed for histology.

2.3.3. Data Analysis

Electrophysiological data analysis was performed by a custom-made MATLAB program. The recorded animal motion data were used to identify phases in the measurement when there was no leg movement. A 30 s long segment was selected from every measurement, when the subject remained motionless. The SNR was calculated based on the work of Lecomte et al.^[46] as $SNR = A / 2 \cdot SD_{noise}$, where A is the peak-to-peak value of the filtered data. The filter of the raw data contained a 200 Hz lowpass filter (5th order Butterworth) and a 1 Hz highpass filter (3rd order Butterworth). The noise was derived from the difference of the raw data and the filtered data, and its standard deviation was calculated to determine the SNR.

2.4. Immunohistochemistry

The physiological state of the neuronal population and astrogliosis was examined to validate the biocompatibility of the device.

2.4.1. Brain Tissue Preparation

In vitro immunohistochemical labeling was carried out post-mortem, 80 days after implantation on average, in three mice. Transcardial perfusion was performed with 0.9% NaCl until liver and lung destained, followed by 4% paraformaldehyde (PFA) solution for 20 min. Picric acid solutions were not used. Following 20 min of perfusion the brain was removed after detaching the electrode grid from the cortical surface. The brain

was postfixed in 4% PFA solution until histological staining was performed.

2.4.2. Immunofluorescent Labeling

Samples were immersed in 30% sucrose solution (in PBS) at 4 °C at least overnight or until the tissue was completely saturated. Coronal sections (cryo, 40 μm thick) were made on a sliding microtome (Leica SM2010 R) and stored in 24-well plates in 1% PBS with 0.3% Sodium Azide. Free-floating sections were washed 3 times for 10 min with 1X PBS, then blocked for an hour at room temperature in a blocking buffer (5% Bovine Serum Albumin, Thermo Scientific) containing 0.3% Triton-X (Sigma-Aldrich) for membrane permeabilization. After blocking and 3 subsequent 10 min washing steps, first with 0.3% Triton-X, then with 1% PBS, GFAP primary antibody was applied directly. Slices were kept at 4 °C overnight before 3 additional 10 min washing steps and the application of the species-specific secondary antibody. In addition to the secondary antibody, fluorescent Nissl stain was applied to the tissue sections for 2 h at room temperature. Unbound secondary antibodies were then washed off with 1% PBS (3 × 10 min). Sections were mounted using 4',6-diamidino-2-phenylindole (DAPI) containing Fluoromount-G (#00-4959-52, Invitrogen) mounting medium to colabel total cell nuclei after rinsing with 1% PBS. Slides were stored at 4 °C in darkness until immunofluorescent imaging was performed the next day.

2.4.3. Antibodies and Imaging

Free-floating sections were stained using the following primary antibodies: fluorescent Nissl stain (NeuroTrace) (1:200, #N21480, Invitrogen) and chicken anti-GFAP (1:2500, #PA1-10004, Invitrogen). GFAP was labeled with species-specific secondary antibody (5 μg mL⁻¹, goat antichick Alexa Fluor 647, #A-21449, Invitrogen). Immunofluorescent imaging was made 2 days after staining using a 20X objective on a Slide Scanner (Pannoramic MIDI II, 3DHISTECH) under blue (DAPI-Q filter) green (FITC-Q filter) and far red (Cy5-Q filter) illumination. Following the acquisition, images were processed using Case Viewer (3DHISTECH) and images were exported at 300 dpi in TIFF file format.

2.4.4. Image Analysis and Statistics

To perform statistical analysis on the immunostained samples, the position of the device was determined on the surface of the cortex manually using Case Viewer (3DHISTECH). Cortical layers I – II/III were distinguished from layer V by the location of giant pyramidal cells.^[47] Bilateral cortical areas were annotated in a manner that the marked regions were both rectangular, $500 \times 500 \mu\text{m}$ and placed at the same distance from the midline at the border of layers IV and V, so that they would be the exact reflections of each other, thus suitable for comparison. As reference for cortical layer distinction, nuclei of giant pyramidal cells were stained among every cell nucleus with DAPI. Sample regions of the cortex were annotated on sections covered with the implanted device both on the implantation side and the intact contralateral hemisphere, which served as primary control. Image analysis was carried out with custom code in MATLAB (Mathworks). Analysis was performed for each labeling separately. Average background intensity was calculated from a separate annotation, subtracted from exported sample annotations and negative valued pixels of samples were then discarded. Average intensities of electrode-side and contralateral side samples of sections were then compared with Student's paired *t*-test. To quantify the difference between cell populations under the implant and the contralateral hemisphere, the number of nuclei was counted using the ITCN

plugin in ImageJ on DAPI stained annotated regions, then compared with Student's paired *t*-test. As manual cortical thickness measurements can lead to inaccuracy, a custom, MATLAB based method was used. As sample annotations placed to the border of layers IV and V extended beyond layer I and included background due to their size, the ratio of tissue and background pixels were used to compare cortical thickness between hemispheres. The 95th percentile of the pixel distribution of background annotations was used as the threshold value in sample annotations.

3. Results

3.1. Electrochemical Performance

Results of long-term electrochemical impedance spectroscopy measurements are summarized in **Figure 3**. Bode plots of a representative μECoG array recorded immediately after immersion (Figure 3A) and on the 16th day (Figure 3B) (frequency range: 1 Hz–10 kHz). Impedance dropped from the initial value $733 \pm 1.93 \text{ k}\Omega$ ($n = 31$) to $5.54 \pm 0.49 \text{ k}\Omega$ ($n = 31$) between the 2nd and the 6th day of the soaking experiment and stabilized thereafter, while the arrays were constantly soaked in 0.01 M PBS solution. At the last day of the stability experiment, recorded impedance was $5.31 \pm 0.50 \text{ k}\Omega$. Phase angle switched from

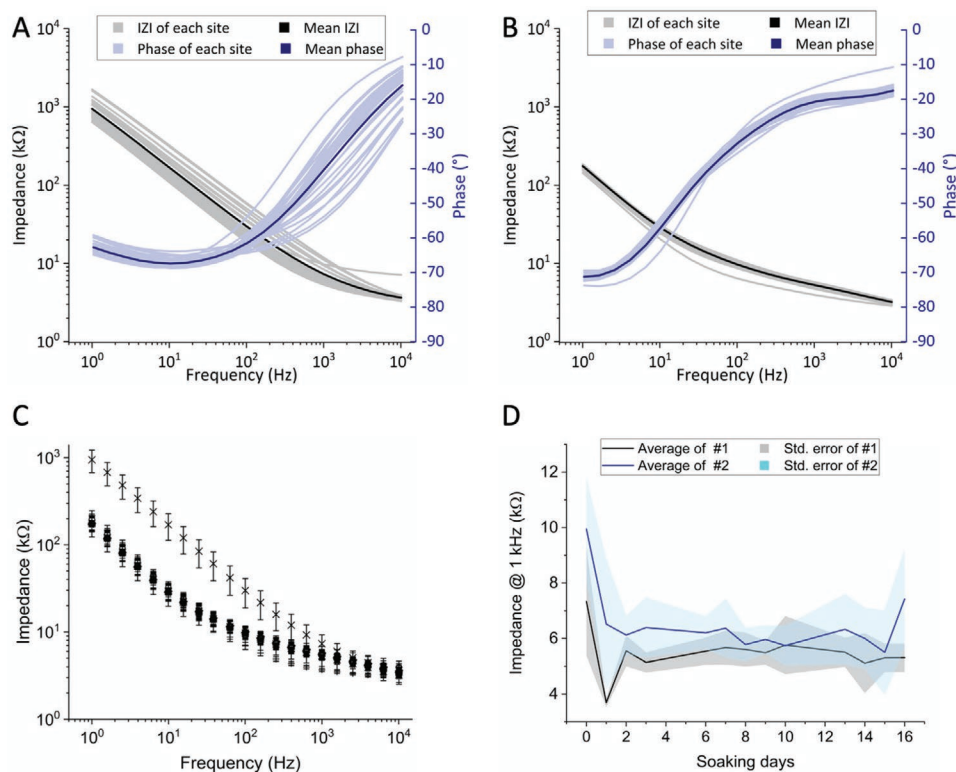


Figure 3. Electrochemical impedance spectroscopy. A,B) Pale gray lines represent the impedance; pale blue lines represent the phase across the 1 Hz–10 kHz frequency range for all functional electrode sites immediately after immersion A) and on the 16th day B) of soaking test. Thick black lines and thick blue lines represent the average of all functional electrode sites respectively. C) Impedance of all frequencies (1 Hz–10 kHz) for a representative μECoG array at 13 time points (Mean of each electrode \pm standard error: initial (X), 1st (+), 2nd (O), 3rd (□), 6th (Δ), 7th (▽), 8th (◇), 9th (◁), 10th (▷), 13th (○), 14th (☆), 15th (◇), 16th (*)) day of EIS test period. D) Average impedance (thick black and blue lines) at 1 kHz on two different but functionally identical mECoG devices. Shaded areas represent the standard error.

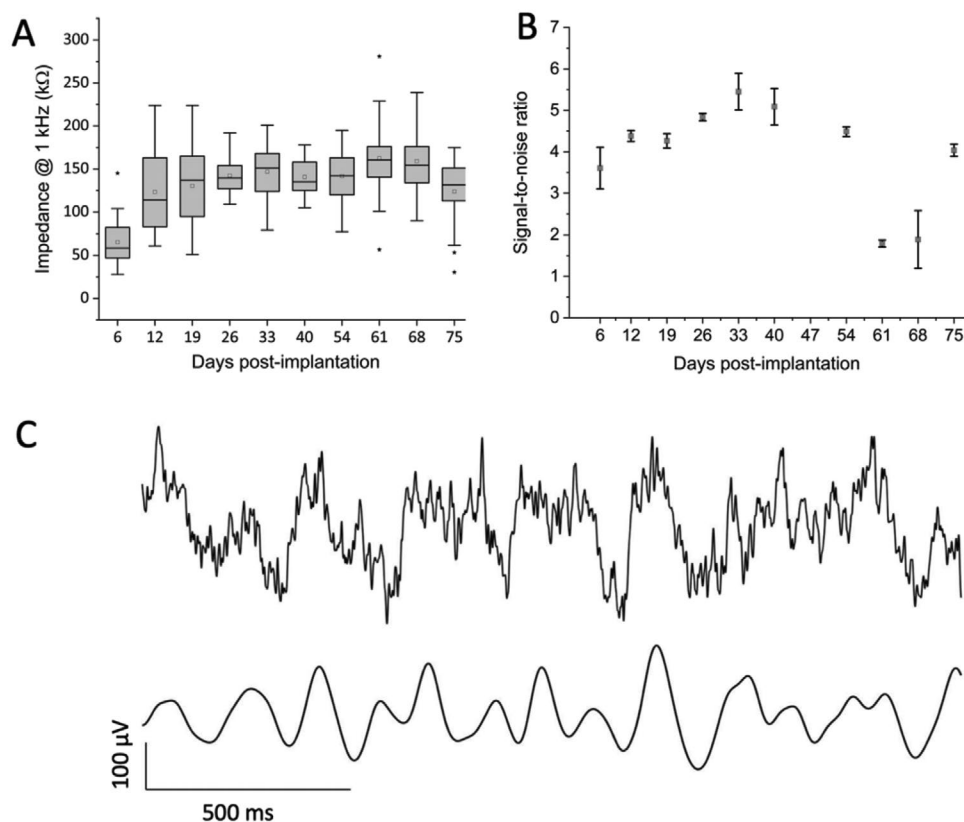


Figure 4. A) Post-implantation impedance of one device at 1 kHz. Acceptance limit as a functional electrode was 400 kΩ. Post-implantation data are from $n = 24$ electrodes of the same representative device. Impedance magnitude increased over time from day 6 until day 61, then started to decrease. B) SNR at ten time points ($n = 24$). Data are shown as mean \pm standard error. C) 2 s long filtered ECoG signal from a representative electrode at the 33rd day post-implantation and the theta range (3.5–11 Hz) of the signal. In A–C), data were collected and analyzed from the same experimental animal (#2).

$-40.0 \pm 6.9^\circ$ to $-18.5 \pm 2.5^\circ$ on the 6th day and remained stable during the experimental period. As expected, the equivalent circuit analysis revealed that the resistance of the bulk electrolyte (R_s) did not change during the testing period, while the constant phase element (CPE) and the frequency-dependent constant, α showed a slight decrease in the first 2 days. These findings suggest that electrode behavior and conductivity are dominated by resistance. Uniform decrease in the impedance (Figure 3C), changes in the value and characteristics of phase curves mainly at higher frequency ranges, and the reduction of CPE with α all indicate a possible penetration of electrolyte throughout polymer layers. Magnitude of impedance of two individual μ ECoG devices at 1 kHz is shown in Figure 3D. Both arrays show similar characteristics, which proves the reliability of material composition, the applied microfabrication processes, and the proposed packaging procedure. The electrochemical impedance spectroscopy confirms that the impedance of SIROF microelectrodes is low and stable enough to test their in vivo performance and measure neural activities of mouse cerebral cortex subdurally.

3.2. Impedance Change and Electrode Yield During Chronic Experiment

In vivo experiments were designed to demonstrate reliable neural implant functionality. The chronic recording performance

of the cortical thiol-ene/acrylate μ ECoG device was evaluated (Figure 4). Electrophysiological recording capability of SIROF electrodes were studied in awake, freely moving, head-fixed mice on a weekly basis. Representative ECoG data (Figure 4C) show characteristic theta rhythms (3.5–11 Hz). Average post-implantation SNR ranged from 1.04 to 5.74 on three different μ ECoGs (Figure 4B). Functional electrode yield decreased to 75% after implantation, but no additional loss was observed throughout the rest of the in vivo experiment (Figure S2, Supporting Information). The acceptance criteria that we identified was that the upper impedance limit was set to 400 kΩ, above this the electrode was considered as nonfunctional. Figure 4A shows mean impedance of representative traces at 1 kHz measured from a single device prior to implantation (in artificial cerebrospinal fluid, aCSF), and 6, 12, 19, 26, 33, 40, 54, 61, 68, 75 days following implantation. All functional electrodes exhibited an increase in impedance 6 days post-implantation (73.10 ± 27.81 kΩ, $n = 24$) versus benchtop measurement in Ringer's solution, performed immediately before the implantation (16.56 ± 2.62 kΩ, $n = 28$). There was an additional increase in impedance 12 days post-implantation (127.72 ± 52.73 kΩ, $n = 24$), which remained relatively consistent at this value and increased only slightly through the first 61 days. Impedance started to decrease on the 68th day, then approached its value measured after 12 days post-implantation. Functional electrodes (<400 kΩ) were selected for electrophysiological recordings.

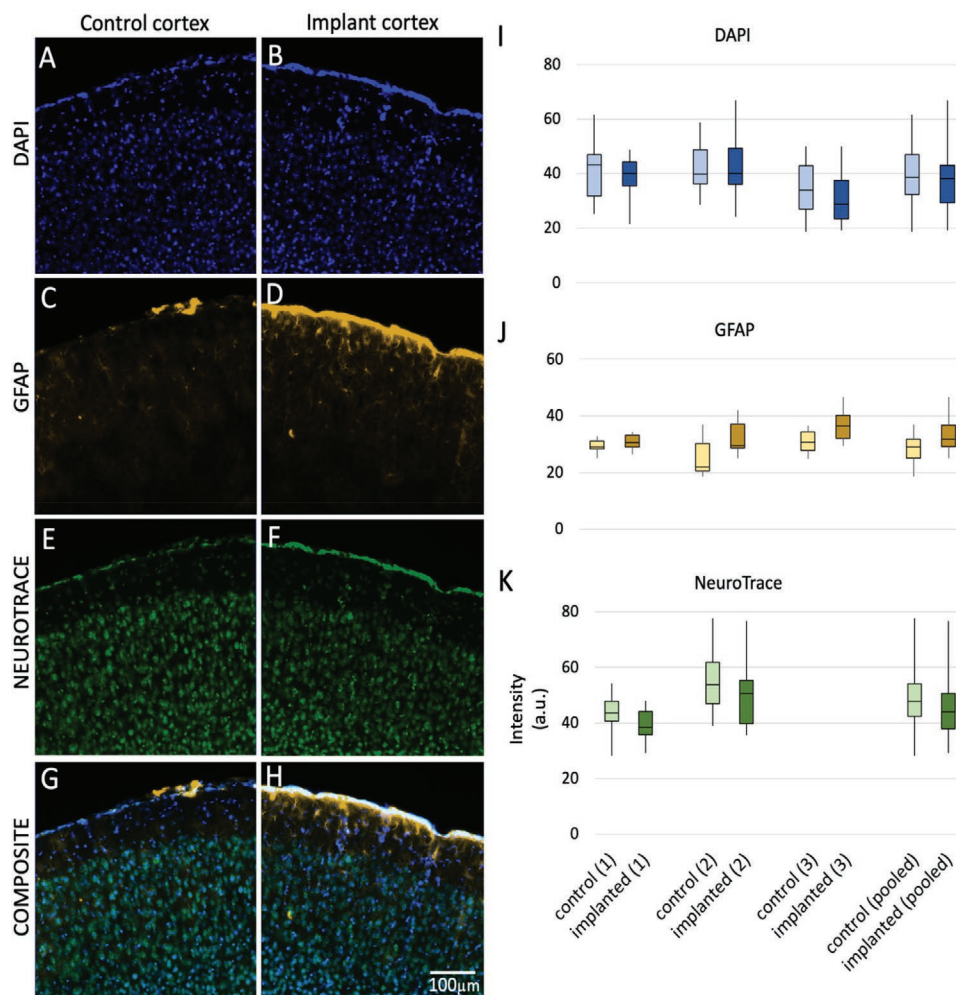


Figure 5. Fluorescent images of thiol-ene/acrylate μ ECoG implanted brains after 80 days of chronic implantation. Images show layers I–IV of the mouse cortex. A,B) Cell nuclei stained with DAPI. C,D) Astrocytes stained with GFAP. E,F) Neurons stained with NeuroTrace, a fluorescent Nissl stain. G,H) Composite images of the three stains. I) Box plots showing minimum, quartiles, mean and maximum of DAPI staining intensity for control and implanted cortices in three subjects and averaged. J) Same as I), for GFAP staining. K) Same as I), for NeuroTrace staining in 2 subjects.

3.3. Immunohistochemistry

To evaluate the impact caused by the long-term chronic implantation of the designed thiol-ene/acrylate probe, histology targeting astrocytes (GFAP) and the physiological state of neurons (NeuroTrace) was performed after 80 days of implantation on average, in three mice. **Figure 5** shows representative fluorescent images for each marker and the calculated fluorescent intensity of the implanted and contralateral hemisphere, which functioned as primary control. For secondary control, only a glass coverslip was implanted to one subject, without probe implantation.

Compared to primary control, there was no significant difference in the intensity and number of cell nuclei (DAPI), while the difference of GFAP intensity was highly significant, indicating that after 10 weeks of implantation, repairing and scarring mechanisms were in progress. The highly significant increase in the intensity of NeuroTrace staining (measured in 2 of 3 mice due to technical difficulties) reflects the consistent high protein synthesis capacity of neuronal cells, as in injured

or regenerating neurons, Nissl substance is redistributed around the periphery of the cell body. Secondary controls supported the results of the primary control (Figure S4, Supporting Information).

4. Discussion

Prior to the present study, the use of softening polymers was limited to intracortical microprobes. Vitale et al.^[25] presented a biomimetic extracellular matrix film as a hydrogel coating to improve the chronic biocompatibility of microfabricated subdural microelectrode arrays. In their dry state, hydrogels express Young's modulus in the GPa range (e.g., 3.4 GPa^[16]). However, when they are exposed to the aqueous environment of the intracranial space, even a few MPa (e.g., 2.6 MPa^[16]) is achievable. The main drawback (and controversially, the greatest appeal) of hydrogels is their excessive water absorption. Their swelling rate varies between 10% and 70%, which is an additional risk for structural degradation and metal

delamination. Swelling also distances recording sites from active neurons and increases intracranial pressure. Newly engineered softening polymer materials undergo stimuli responsive transition (e.g., temperature, ion concentration, pH, aqueous environment) when they are exposed to the extracellular space. Like hydrogels, softening polymer materials maintain their mechanical robustness (Young's modulus in the GPa range) during implantation, thus providing easy handling before and after neurosurgeries. Thermoset softening polymers that can be tuned to undergo glass transition at physiological temperature (37 °C) are currently being investigated.^[38–41] Even though SMPs are very popular among researchers performing in vivo studies, they mainly focus on SMP coated needle electrodes. Using SMP as a carrier material for μ ECoG devices in chronic experiments is a yet undiscovered area and is of great interest, as it may mitigate foreign body response.

For the reasons listed above, our study focused on a new thiol-ene/acrylate μ ECoG device specifically designed for chronic cortical experiments. Thiol-ene/acrylate compositions have been shown to undergo remarkable changes in elastic properties, softening from over 1 GPa to 300 MPa with less than 3% fluid uptake upon exposure to PBS at 37 °C. Based on its beneficial properties as a flexible and compliant substrate material, we hypothesized that the use of thiol-ene/acrylate is advantageous for μ ECoG devices. The presented device has 31 SIROF recording sites in a symmetric layout, and it was designed to address the challenges of combined experiments with neuroimaging techniques, where a cranial window is also necessary.

To evaluate the reliability of the packaging method and to test the electrochemical stability of μ ECoG devices over time, we performed EIS measurements on different, but functionally equal arrays across all electrodes for 16 days (Figure 3). Impedance and phase angle analysis revealed that the packaging procedure resulted in 29 functional electrodes out of the designed 31 on average. Impedance decreased during the first few days after the soaking period started and stabilized between the 6th and 8th day. Uniform decrease in impedance, increase in phase angle and the equivalent circuit analyses all support the idea that diffusion of solvent occurred into the polymer layers.^[39,48] This would undermine the electrophysiological performance of the device except for Parylene C, which was used as an additional layer in the microdevice to prevent the formation of shortcuts between conductive traces.

In vivo electrophysiological recordings were carried out on all functional electrodes weekly after EIS. Although electrode yield decreased after implantation by 25%, we observed no additional loss in active electrode yield over the 75-day measurement period (Figure S2, Supporting Information). Impedance increased after implantation compared to pre-implantation, most likely in association with acute inflammation. Impedance approached its highest value after 61 days, then started to decrease until the 75th day when the magnitude of impedance was similar to what we measured after 12 days (Figure 4A). Stiller et al.^[41] reported similar results with thiol-ene/acrylate shape memory polymer probes. The SNR values are comparable to those of DC sputtered platinum electrodes on polyimide μ ECoG (8.9^[49]). With the same SNR calculating method, silicon-based arrays were examined^[50] and in this previous study, a signal quality scale was defined, according to which our

device would have a “fair” signal quality. Since this grouping was defined for penetrating electrode arrays, the SNR of our μ ECoG is appropriate. In vivo results validated the reliable functionality of μ ECoGs fully encapsulated with SMP.

We observed an increased GFAP signal in the immunohistochemical staining under the implanted device compared to the contralateral cortex of the same animal, which indicated that foreign body response may still be in progress 80 days after implantation. Beside this, there was an unusually high protein synthesis made visible by NeuroTrace labeling. Compared to the primary control, there was no significant difference in DAPI signal intensity, which was supported by cell counting. Histology from coverglass implanted animals (secondary control) confirmed that this increase is likely not due to the presence of the device. This implies that the increase in astrocyte activity and protein synthesis is due to the surgical procedure (e.g., removal of *dura mater*) and the use of coverglass as a substitute of skull bone (Figure S3, Supporting Information). Furthermore, it is clear on the fluorescent images that the electrode-cortex interface was dominated by GFAP astrocytes (Figure 5D). This finding is in good agreement with the work of Saxena et al., who found the same high appearance of GFAP astrocytes at the electrode-cortex interface 16 weeks post-implantation in rats.^[51] Moreover, Ravikumar et al. found that GFAP immunoreactivity was the highest at 2- and 16-weeks post-implantation in mice but concluded that they did not find any correlation between neurodegeneration and activated microglia, which supports our findings in terms of cell numbers.^[52]

5. Conclusion

We introduced a newly designed microECoG device featuring the shape memory polymer thiol-ene/acrylate as an encapsulating substrate. Using SMP as a carrier material for μ ECoG devices in chronic experiments for the first time, we presented the electrochemical performance of the device in a wide range of tests including long-term in vivo conditions. Chronic experiments require the stability of recording quality for optimal utility. We measured electrode impedance over a period of 75 days to characterize the electrode yield. Impedance increased markedly after implantation, resulting in loss of only 25% of electrodes. However, it remained virtually unchanged over 60 days until the end of the experiment, with 75% of electrodes remaining under 400 k Ω . Excellent recording quality was reflected by high SNR throughout the course of the experiment, as well as by readily discernible theta oscillations in sample recordings. Immunohistochemical staining supported the biocompatibility of the device, as cortical thickness measurements showed no significant difference between implanted and control cortices. GFAP and NeuroTrace labeling confirmed the ongoing foreign body response after 80 days of implantation, as well as altered protein synthesis. Surgery controls without ECoGs confirmed that these changes are not caused by the implanted device, but instead may be due to the removal of the *dura mater*, which requires further investigation.

Designed with the purpose of combined recordings of calcium sensors and ECoG in mind, our novel device may allow concurrent two-photon imaging and electrocorticography in the future.

Supporting Information

Supporting Information is available from the Wiley Online Library or from the author.

Acknowledgements

F.Z.F., M.M. and A.Z. contributed equally to this work. The authors are grateful for the funding of the National Development and Innovation Office (Nos. NKFIH FK 134403 and TKP2020-NKA-11 to Z.F.) and the support of the Hungarian Brain Research Program (No. 2017_1.2.1_NKP-2017-00002). This work was supported by the European Research Council (ERC) Grant Nos. 682426, KFI-2018-00097, VKE-2018-00032, VKSZ, and 712821-NEURAM for B.R., the Bolyai Fellowship of the Hungarian Academy of Sciences for Z.F., and the ÚNKP-20-3 New National Excellence Program of the Ministry for Innovation and Technology from the source of the National Research, Development and Innovation Fund (No. ÚNKP-20-3-II-PPKE-28) for Á.Sz. The supporting grammatical work of Rózsa Flóra Várady-Szabó was highly appreciated.

Conflict of Interest

The authors declare no conflict of interest.

Data Availability Statement

Research data are not shared.

Keywords

responsive polymers, neural implants, microECoG, electrophysiology, biocompatibility

Received: August 2, 2021
Revised: September 9, 2021
Published online:

- [1] B. Burle, L. Spieser, C. Roger, L. Casini, T. Hasbroucq, F. Vidal, *Int. J. Psychophysiol.* **2015**, *97*, 210.
- [2] G. Buzsáki, X.-J. Wang, *Annu. Rev. Neurosci.* **2012**, *35*, 203.
- [3] G. Schalk, E. C. Leuthardt, *IEEE Rev. Biomed. Eng.* **2011**, *4*, 140.
- [4] L. Muller, J. D. Rolston, N. P. Fox, R. Knowlton, V. R. Rao, E. F. Chang, *J. Neural Eng.* **2018**, *15*, 026015.
- [5] G. Buzsáki, C. A. Anastassiou, C. Koch, *Nat. Rev. Neurosci.* **2012**, *13*, 407.
- [6] Y. Lu, X. Liu, R. Hattori, C. Ren, X. Zhang, T. Komiyama, D. Kuzum, *Adv. Funct. Mater.* **2018**, *28*, 1800002.
- [7] W. S. Konerding, U. P. Froriep, A. Kral, P. Baumhoff, *Sci. Rep.* **2018**, *8*, 3825.
- [8] A. Zátanyi, Z. Borhegyi, D. Cserpán, Z. Somogyvári, M. Srivastava, Z. Kisvárdy, Z. Fekete, *Proceedings* **2017**, *1*, 610.
- [9] A. Zátanyi, M. Madarász, O. Szabó, T. Lőrincz, R. Hodován, B. Rózsa, Z. Fekete, *J. Neural Eng.* **2020**, *17*, 016062.
- [10] C. Hébert, E. Masvidal-Codina, A. Suarez-Perez, A. B. Calia, G. Piret, R. Garcia-Cortadella, X. Illa, E. Del Corro Garcia, J. M. De la Cruz Sanchez, D. V. Casals, E. Prats-Alfonso, J. Bousquet, P. Godignon, B. Yvert, R. Villa, M. V. Sanchez-Vives, A. Guimerà-Brunet, J. A. Garrido, *Adv. Funct. Mater.* **2018**, *28*, 1703976.
- [11] C. Marin, E. Fernández, *Front. Neuroeng.* **2010**, *3*, 8.
- [12] C. Kim, J. Jeong, S. J. Kim, *Sensors* **2019**, *19*, 1069.
- [13] J. P. Harris, J. R. Capadona, R. H. Miller, B. C. Healy, K. Shanmuganathan, S. J. Rowan, C. Weder, D. J. Tyler, *J. Neural Eng.* **2011**, *8*, 066011.
- [14] A. Gilletti, J. Muthuswamy, *J. Neural Eng.* **2006**, *3*, 189.
- [15] Z. Bérces, K. Tóth, G. Márton, I. Pál, B. Kováts-Megyési, Z. Fekete, I. Ulbert, A. Pongrácz, *Sci. Rep.* **2016**, *6*, 35944.
- [16] A. Lecomte, E. Descamps, C. Bergaud, *J. Neural Eng.* **2018**, *15*, 031001.
- [17] M. Jorfi, J. L. Skousen, C. Weder, J. R. Capadona, *J. Neural Eng.* **2015**, *12*, 011001.
- [18] K. J. Yu, D. Kuzum, S. W. Hwang, B. H. Kim, H. Juul, N. H. Kim, S. M. Won, K. Chiang, M. Trumpis, A. G. Richardson, H. Cheng, H. Fang, M. Thompson, H. Bink, D. Talos, K. J. Seo, H. N. Lee, S. K. Kang, J. H. Kim, J. Y. Lee, Y. Huang, F. E. Jensen, M. A. Dichter, T. H. Lucas, J. Viventi, B. Litt, J. A. Rogers, *Nat. Mater.* **2016**, *15*, 782.
- [19] J. Pas, A. L. Rutz, P. P. Quilichini, A. Sl, A. Ghemest, A. Kaszas, M. J. Donahue, V. F. Curto, R. P. O. Connor, C. Bernard, A. Williamson, G. G. Malliaras, *J. Neural Eng.* **2018**, *15*, 065001.
- [20] Z. Fekete, A. Pongrácz, *Sens. Actuators, B* **2017**, *243*, 1214.
- [21] S. Wurth, M. Capogrosso, S. Raspopovic, J. Gandar, G. Federici, N. Kinany, A. Cutrone, A. Piersigilli, N. Pavlova, R. Guiet, G. Taverni, J. Rigosa, P. Shkorbatova, X. Navarro, Q. Barraud, G. Courtine, S. Micera, *Biomaterials* **2017**, *122*, 114.
- [22] F. Wu, M. Im, E. Yoon, *2011 16th Int. Solid-State Sensors, Actuators Microsystems Conf. TRANSDUCERS'11*, IEEE, New York **2011**, pp. 966–969.
- [23] A. Zátanyi, Z. Borhegyi, M. Srivastava, D. Cserpán, Z. Somogyvári, Z. Kisvárdy, Z. Fekete, *Sens. Actuators, B* **2018**, *273*, 519.
- [24] G. Márton, G. Orbán, M. Kiss, R. Fiáth, A. Pongrácz, I. Ulbert, *PLoS One* **2015**, *10*, e0206137.
- [25] F. V. Id, W. Shen, N. Driscoll, J. C. Burrell, G. Richardson, O. Adewole, B. M. Id, A. A. Id, H. Oh, T. Wang, T. H. Lucas, D. K. Cullen, M. G. Allen, B. Litt, *PLoS One* **2018**, *13*, 1.
- [26] D. W. Park, S. K. Brodnick, J. P. Ness, F. Atry, L. Krugner-Higby, A. Sandberg, S. Mikael, T. J. Richner, J. Novello, H. Kim, D. H. Baek, J. Bong, S. T. Frye, S. Thongpang, K. I. Swanson, W. Lake, R. Pashaie, J. C. Williams, Z. Ma, *Nat. Protoc.* **2016**, *11*, 2201.
- [27] D. Khodagholi, J. N. Gelinis, T. Thesen, W. Doyle, O. Devinsky, G. G. Malliaras, G. Buzsáki, *Nat. Neurosci.* **2015**, *18*, 310.
- [28] J. Zhang, X. Liu, W. Xu, W. Luo, M. Li, F. Chu, L. Xu, A. Cao, J. Guan, S. Tang, X. Duan, *Nano Lett.* **2018**, *18*, 2903.
- [29] I. R. Mineev, P. Musienko, A. Hirsch, Q. Barraud, N. Wenger, E. M. Moraud, J. Gandar, M. Capogrosso, T. Milekovic, L. Asboth, R. F. Torres, N. Vachicouras, Q. Liu, N. Pavlova, S. Duis, A. Larmagnac, J. Vörös, S. Micera, Z. Suo, G. Courtine, S. P. Lacour, *Science* **2015**, *347*, 159.
- [30] G. Hotson, D. P. McMullen, M. S. Fifer, M. S. Johannes, K. D. Katyal, M. P. Para, R. Armiger, W. S. Anderson, N. V. Thakor, B. A. Wester, N. E. Crone, *J. Neural Eng.* **2016**, *13*, 026017.
- [31] D.-H. Baek, J. Lee, H. J. Byeon, H. Choi, K. I. Young, K.-M. Lee, P. J. Jungho, J. D. Pyo, S.-H. Lee, *J. Neural Eng.* **2014**, *11*, 046023.
- [32] B. Rubehn, C. Bosman, R. Oostenveld, P. Fries, T. Stieglitz, *J. Neural Eng.* **2009**, *6*, 036003.
- [33] F. Wu, L. W. Tien, F. Chen, J. D. Berke, D. L. Kaplan, *J. Microelectromech. Sys.* **2015**, *24*, 62.
- [34] S. Watanabe, H. Takahashi, K. Torimitsu, *Jpn. J. Appl. Phys.* **2017**, *56*, 037001.
- [35] G.-L. Li, J.-T. Wu, Y.-H. Xia, Q.-G. He, H.-G. Jin, *J. Neural Eng.* **2020**, *17*, 051004.
- [36] H. Toda, T. Suzuki, H. Sawahata, K. Majima, Y. Kamitani, I. Hasegawa, *Neuroimage* **2011**, *54*, 203.
- [37] L. Macdougall, H. Culver, C.-C. Lin, C. Bowman, K. Anseth, *Chapter in Biomaterials Science*, 4th ed., **2020**, pp. 167–190.
- [38] D. M. Simon, H. Charkhar, C. St John, S. Rajendran, T. Kang, R. Reit, D. Arreaga-Salas, D. G. McHail, G. L. Knaack, A. Sloan,

- D. Grasse, T. C. Dumas, R. L. Rennaker, J. J. Pancrazio, W. E. Voit, *J. Biomed. Mater. Res., Part A* **2017**, *105*, 159.
- [39] A. Zátónyi, G. Orbán, R. Modi, G. Márton, D. Meszéna, I. Ulbert, A. Pongrácz, M. Ecker, W. E. Voit, A. Joshi-Imre, Z. Fekete, *Sci. Rep.* **2019**, *9*, 2321.
- [40] C. L. Frewin, M. Ecker, A. Joshi-Imre, J. Kamgue, J. Waddell, V. R. Danda, A. M. Stiller, W. E. Voit, J. J. Pancrazio, *Polymers* **2019**, *11*, 902.
- [41] A. M. Stiller, J. Usoro, C. L. Frewin, V. R. Danda, M. Ecker, A. Joshi-Imre, K. C. Musselman, W. Voit, R. Modi, J. J. Pancrazio, B. J. Black, *Micromachines* **2018**, *9*, 500.
- [42] G. Li, S. Wang, Y. Y. Duan, *Sens. Actuators, B* **2018**, *277*, 250.
- [43] G. Li, S. Wang, M. Li, Y. Y. Duan, *J. Neural Eng.* **2021**, *18*, 046016.
- [44] A. Campbell, C. Wu, *Micromachines* **2018**, *9*, 430.
- [45] A. D. Degenhart, J. Eles, R. Dum, J. L. Mischel, I. Smalianchuk, B. Endler, R. C. Ashmore, E. C. Tyler-Kabara, N. G. Hatsopoulos, W. Wang, A. P. Batista, X. T. Cui, *J. Neural Eng.* **2016**, *13*, 046019.
- [46] A. Lecomte, A. Degache, E. Descamps, L. Dahan, C. Bergaud, *Sens. Actuators, B* **2017**, *251*, 1001.
- [47] M. Matelli, G. Luppino, G. Rizzolatti, *J. Comp. Neurol.* **1991**, *311*, 445.
- [48] P. Takmakov, K. Ruda, K. Scott Phillips, I. S. Isayeva, V. Krauthamer, C. G. Welle, *J. Neural Eng.* **2015**, *12*, 026003.
- [49] A. Zátónyi, F. Fedor, Z. Borhegyi, Z. Fekete, *J. Neural Eng.* **2018**, *15*, 054003.
- [50] S. Suner, M. R. Fellows, C. Vargas-Irwin, G. K. Nakata, J. P. Donoghue, *IEEE Trans. Neural Syst. Rehabil. Eng.* **2005**, *13*, 524.
- [51] T. Saxena, L. Karumbaiah, E. A. Gaupp, R. Patkar, K. Patil, M. Betancur, G. B. Stanley, R. V. Bellamkonda, *Biomaterials* **2013**, *34*, 4703.
- [52] M. Ravikumar, S. Sunil, J. Black, D. S. Barkauskas, A. Y. Haung, R. H. Miller, S. M. Selkirk, J. R. Capadona, *Biomaterials* **2014**, *35*, 8049.